Research Square

Preprints are preliminary reports that have not undergone peer review.
They should not be considered conclusive, used to inform clinical practice,
or referenced by the media as validated information.

GPU-Accelerated Direct Numerical Simulation of Non-premixed syngas/air Flame

Edoardo Forti

edoardo.forti@uniroma1.it

Sapienza University of Rome

Mauro Valorani

Sapienza University of Rome

Agostino Neri

European Space Agency

Matteo Bernardini

Sapienza University of Rome

Pietro Paolo Ciottoli

Sapienza University of Rome

Research Article

Keywords: Direct Numerical Simulation, Chemical kinetics, High performance computing, Turbulent reacting flows

Posted Date: November 13th, 2026

DOI: https://doi.org/10.21203/rs.3.rs-11492665/v1

License: This work is licensed under a Creative Commons Attribution 4.0 International License.
Read Full License

Additional Declarations: No competing interests reported.

GPU-Accelerated Direct Numerical Simulation of Non-premixed syngas/air Flame

Edoardo Forti[1*], Mauro Valorani[1], Agostino Neri[2], Matteo Bernardini[1], Pietro Paolo Ciottoli[1]

[1*]Department of Mechanical and Aerospace Engineering, Sapienza, University of Rome, Via Eudossiana, 18, Rome, 00184, Lazio, Italy.
[2]European Space Agency, Via Galileo Galilei, 1, Frascati, 00044, Lazio, Italy.

*Corresponding author(s). E-mail(s): edoardo.forti@uniroma1.it;
Contributing authors: mauro.valorani@uniroma1.it;
agostino.neri@esa.int; matteo.bernardini@uniroma1.it;
pietropaolo.ciottoli@uniroma1.it;

Abstract

A direct numerical simulation (DNS) of the Sandia/ETH-Zurich $CO/H_2/N_2$ flame A, a turbulent non-premixed syngas/air jet flame at a Reynolds number of 16700, is presented. The computation is performed with the GPU-accelerated compressible solver STREAmS-2.0 on a grid of approximately 3.43 billion points, with detailed finite-rate chemistry and mixture-averaged molecular transport, and covers a laboratory-scale domain. Since the experimental inlet velocity profile is not fully documented, the turbulent inflow is prescribed analytically and calibrated on the declared bulk velocity. The statistical profiles reproduce the experimental data but exhibit a systematic axial shift, which is attributed to the residual uncertainty in the inflow specification; once the shift is accounted for, mean, RMS, and conditional statistics agree closely with the measurements. Every element of the setup is analytical and the complete statistical database is provided as Supplementary Material, so that the simulation is fully reproducible and is proposed as a numerical benchmark for the validation of reacting-flow solvers and combustion models.

Keywords: Direct Numerical Simulation, Chemical kinetics, High performance computing, Turbulent reacting flows

1 Introduction

Synthesis gas (syngas), a mixture of hydrogen and carbon monoxide typically diluted with nitrogen, carbon dioxide, and water vapor, can be obtained from the gasification of coal, biomass, or waste. It serves as the primary fuel in integrated gasification combined cycle (IGCC) power plants, where gasification enables pre-combustion carbon dioxide capture to reduce emissions from solid feedstocks (Lieuwen et al. 2009). Syngas has also attracted attention as a hydrogen-rich alternative to fossil fuels in internal combustion engines (Yaliwal et al. 2014; Paykani et al. 2022) and gas turbines (Gupta et al. 2010; Ghenai 2010; Gadde et al. 2006). While H_2/CO mixtures retain the high flame speeds and wide flammability limits of pure hydrogen, the carbon monoxide moderates the overall reactivity and reduces flashback propensity (Sung and Law 2008). The oxidation kinetics of syngas are well understood; the H_2/O_2 and $CO/H_2/O_2$ subsystems form the foundation upon which larger hydrocarbon reaction mechanisms are hierarchically constructed (Varga et al. 2016). Turbulent non-premixed syngas jet flames have been studied extensively within the International Workshop on Measurement and Computation of Turbulent Nonpremixed Flames (TNF). The Sandia/ETH-Zurich $CO/H_2/N_2$ flame series (Barlow et al. 2000, 2002) is among the best documented configurations of this class. Temperature and species concentrations were measured at Sandia National Laboratories by simultaneous Rayleigh/Raman scattering and laser-induced fluorescence, while the velocity field was characterized at ETH Zurich by three-component laser-Doppler velocimetry. Flame A of the series is a turbulent, attached, unconfined jet flame at $\mathrm{Re} = 16700$. It shows no localized extinction, but flow and chemical time scales overlap appreciably, so the case discriminates well between turbulence–chemistry interaction models. Numerical studies of this configuration include RANS computations based on the eddy dissipation concept and on steady laminar flamelet closures (Lysenko et al. 2014), unsteady simulations (Giacomazzi et al. 2008), and large-eddy simulations, also at elevated pressure (Ciottoli et al. 2020). To the best of the authors' knowledge, no fully resolved direct numerical simulation (DNS) of this flame has been reported so far. The cost of such a computation, set by the laboratory-scale dimensions of the burner and by the moderately high Reynolds number, has simply been out of reach until recently.

DNS resolves all scales of a turbulent reacting flow and therefore requires no subgrid model for turbulence or combustion (Moin and Mahesh 1998). For a long time its cost confined it to canonical configurations of millimeters scale. Petascale and exascale machines have changed the terms of the problem (Chen 2011; Domingo and Vervisch 2023). Solvers written for these architectures, among them the Pele suite (de Frahan et al. 2023), nekCRF (Kerkemeier et al. 2024), and STREAmS (Salvadore et al. 2013; Bernardini et al. 2021), sustain computations with billions of grid points, and DNS of laboratory-scale burners with detailed chemistry have started to appear (Minamoto and Chen 2016; Scialabba et al. 2025). Thus, it has become possible to compare DNS directly with measurements on the very configurations used for model validation. Such a comparison tests the numerical setup and the consistency of the experimental boundary conditions at the same time.

This paper presents a DNS of the Sandia/ETH-Zurich $CO/H_2/N_2$ flame A. The

simulation was performed with the extended version of the GPU-accelerated compressible solver STREAmS-2.0 (Bernardini et al. 2023; Forti et al. 2025) on a grid of approximately 3.43 billion points. Finite-rate chemistry is described by the 14-species ELTE syngas mechanism (Varga et al. 2016), and molecular transport by the mixture-averaged approximation, which accounts for the differential diffusion promoted by the high hydrogen content of the fuel. The computation ran on 398 NVIDIA A100 GPUs and covers a domain of $28.4 \times 18.3 \times 18.3$ cm^3, considerably larger than the domains employed in typical reacting DNS; it ranks among the largest direct numerical simulations of a turbulent reacting flow performed to date.
Every element of the numerical setup is analytical and documented in full. The turbulent inflow consists of synthetic perturbations superimposed on a power-law profile, following the formulation of Pitsch and Steiner (2000), with amplitudes calibrated on the declared experimental bulk velocity. The injector is represented by an immersed-boundary method (IBM) with viscous walls, and ignition is obtained through a localized energy deposition of prescribed analytical form. The simulation can therefore be reproduced without recourse to undocumented inflow databases or precursor computations. The complete set of mean, RMS, and conditional statistics, collected at every diameter along the jet, is provided as Supplementary Material, and the computation is proposed as a documented numerical benchmark for reacting-flow solvers and combustion models, in addition to its physical scope.
The paper is organized as follows: Section 2 describes the governing equations, the numerical methods, the ignition procedure, and the generation of the synthetic turbulent inflow; Section 3 presents the test case, the computational domain, and the grid resolution assessment; Section 4 discusses centerline, radial, and conditional statistics and their comparison with the experimental data; conclusions are drawn in Section 5.

2 Mathematical and Numerical Modelling

2.1 Governing equations and physical models

The numerical simulations are performed with STREAmS-2.0 (Supersonic Turbulent REActing Navier–Stokes Solver), a high-fidelity, GPU-accelerated flow solver developed at Sapienza University of Rome for the direct numerical simulation (DNS) of compressible turbulent reacting flows. A detailed description of the governing equations, physical models, and validation campaign of STREAmS-2.0 is available in the literature (Forti et al. 2025); only the main features are summarized in the following. The solver integrates the fully compressible Navier–Stokes equations for a multicomponent reacting mixture,

$$\frac{\partial}{\partial t}\left(\rho Y_m\right) + \frac{\partial}{\partial x_i}\left[\rho\left(u_i + V_{m,i}\right) Y_m\right] = \dot{\omega}_m, \tag{1}$$

$$\frac{\partial}{\partial t}\left(\rho u_i\right) + \frac{\partial}{\partial x_j}\left(\rho u_i u_j\right) = -\frac{\partial p}{\partial x_i} + \frac{\partial \tau_{ij}}{\partial x_j}, \tag{2}$$

$$\frac{\partial}{\partial t}\left(\rho E\right) + \frac{\partial}{\partial x_j}\left(\rho u_j H\right) = -\frac{\partial q_j}{\partial x_j} + \frac{\partial \tau_{ij} u_i}{\partial x_j}, \tag{3}$$

where $m = 1, \ldots, N_s$ denotes the chemical species index, ρ is the mixture density, Y_m the mass fraction of species m, and u_i the velocity component in the i-th direction. The diffusion velocity $V_{m,i}$ is evaluated through the mixture-averaged approximation of Hirschfelder et al. (1954), so that differential diffusion effects are naturally accounted for. The term $\dot{\omega}_m$ is the net chemical production rate of species m per unit volume, p is the thermodynamic pressure, and E and H denote the total specific energy and enthalpy, respectively, both including the chemical contribution. Finally, q_j and τ_{ij} are the components of the energy flux vector and of the viscous stress tensor. Summation of Eq. (1) over all species recovers the continuity equation for the mixture. The chemical source term in Eq. (1) is modelled through finite-rate Arrhenius kinetics, with reaction types compliant with the ANSYS (2015) CHEMKIN standard. STREAmS-2.0 supports elementary reversible reactions, three-body reactions, and pressure-dependent fall-off reactions described through Lindemann (Lindemann et al. 1922), Troe (Gilbert et al. 1983), and SRI (Stewart et al. 1989) formulations.

2.2 Numerical methods

The convective fluxes are discretized using a fifth-order weighted essentially non-oscillatory (WENO) scheme (Jiang and Shu 1996) for the reconstruction of the variables at the cell interfaces, coupled with the HLLC (Harten-Lax-van Leer-contact) approximate Riemann solver (Toro 2009). This combination guarantees low numerical dissipation of the resolved turbulent structures while providing robust capturing of the steep gradients occurring across the flame front. Temporal integration relies on an operator-splitting strategy that decouples the fluid transport from the chemical kinetics. The convective and diffusive terms are advanced explicitly in time with a third-order Runge-Kutta (RK3) scheme, whereas the chemical source terms, which introduce severe numerical stiffness when detailed kinetics are employed, are integrated point-by-point with a fourth-order implicit Rosenbrock solver.

Large language models were employed exclusively as a coding assistant during the post-processing stage: portions of the scripts used to extract the statistical profiles from the slices and to generate the figures were drafted with the assistance of Gemini (Google). All AI-assisted code was reviewed, tested, and validated by the authors, and the resulting statistics were verified against independently computed reference values. No generative AI was used to produce scientific content, data, or images.

2.3 Ignition via localized energy deposition

Ignition is triggered by a localized energy deposition inspired by laser-induced ignition models (Gargiulo et al. 2019) by modifying the energy source term in the vicinity of the injector. As described in Bernardini et al. (2023), the local temperature within each computational cell is retrieved by inverting the definition of the total energy E; therefore, a localized energy deposition translates into a controlled temperature increase. The source term is designed to exhibit a toroidal spatial distribution located in close proximity to the injector post-tip, according to

$$\dot{Q}(x,y,z,t) = A \max\left(T_{obj} - T,\, 0\right) \Big\{ \tanh\left[\epsilon\left(r(y,z) - r_{int}\right)\right] - \tanh\left[\epsilon\left(r(y,z) - r_{ext}\right)\right] \Big\} \times e^{-\sigma_x (x - x_{obj})^2}\, e^{-\sigma_t (t - t_{obj})^2} \quad (4)$$

where T_{obj} is the target temperature of the deposition, which is switched off where $T \geq T_{obj}$, r_{int} and r_{ext} are the inner and outer radii of the torus, and ϵ controls the sharpness of its edges. The parameters x_{obj} and t_{obj} are the axial position and the time instant of maximum deposition, while σ_x and σ_t set the widths of the spatial and temporal Gaussian profiles, whose standard deviations are $(2\sigma_x)^{-1/2}$ and $(2\sigma_t)^{-1/2}$, respectively.

2.4 Turbulent inflow generation

Since the inlet profile is not documented in the experimental dataset (Barlow et al. 2000, 2002), a synthetic turbulent inflow is prescribed at the fuel injection through an analytical condition applied on an immersed-boundary patch. Following the formulation proposed by Pitsch and Steiner (2000), the turbulent inflow is generated by superimposing rotating helical modes and oscillating axisymmetric perturbations onto a baseline power-law velocity profile,

$$u_{\mathrm{pl}} = U_{\mathrm{patch}} \left(1 - r/R\right)^{1/n}, \quad (5)$$

$$u_{tr} = \sum_{i=1}^{6} B_i \sin\left(\alpha_i + i\phi + \Psi_i t\right) + \sum_{i=7}^{8} B_i \sin\left(\Psi_i t\right), \quad (6)$$

$$u = u_{pl} + u_{tr} = U_{\mathrm{patch}} \left(1 - r/R\right)^{1/n} + \sum_{i=1}^{6} B_i \sin\left(\alpha_i + i\phi + \Psi_i t\right) + \sum_{i=7}^{8} B_i \sin\left(\Psi_i t\right). \quad (7)$$

In Eq. (5), U_{patch} is the peak velocity prescribed at the inflow patch, r is the radial coordinate measured from the centerline of the cylindrical injector, R is the injector radius, ϕ is the azimuthal angle, and n is the power-law exponent. In Eq. (6), the phase shifts α_i, which dictate the azimuthal orientation of each helical mode relative to $i\phi$, and the frequencies Ψ_i are randomly distributed. The amplitudes B_i are calibrated so as to reproduce the time-averaged root-mean-square (RMS) velocity fluctuations u'_{exp} measured at the jet exit; for the present perturbation model, this condition is satisfied by setting $B_i = 0.5\, u'_{exp}$ for all modes $i = 1, \ldots, 8$. In our simulation, only the x-component of the velocity, u, is perturbed.
The values of every parameter adopted for the simulated test case are presented in Sec.

3 Simulation setup

3.1 Test case: the Sandia/ETH-Zurich $CO/H_2/N_2$ flame A

The test case investigated in this work is flame A of the Sandia/ETH-Zurich $CO/H_2/N_2$ dataset (Barlow et al. 2000, 2002), a turbulent, non-premixed, unconfined syngas–air jet flame documented within the framework of the International Workshop on Measurement and Computation of Turbulent Nonpremixed Flames (TNF). Scalar measurements (temperature and concentrations of N_2, O_2, CO, H_2, CO_2, H_2O, OH, and NO) were obtained at Sandia National Laboratories by simultaneous Rayleigh/Raman scattering and laser-induced fluorescence, whereas the velocity field was characterized at ETH Zurich by three-component laser-Doppler velocimetry (Barlow et al. 2002). The flame is attached and does not exhibit localized extinction, yet it features a significant coupling between flow and chemical time scales, which makes it a well-established benchmark for the assessment of turbulence-chemistry interaction models.
For this simulation, the pressure is $P = 1$ atm. The fuel mixture consists of $CO/H_2/N_2$ (40%/30%/30% by volume) at $T_{\text{fuel}} = 292$ K, issuing with a bulk velocity $U_{\text{bulk}} = 76$ m/s, corresponding to a jet Reynolds number $\text{Re} = 16700$ based on the inner injector diameter. The ambient coflow consists of air with a water vapor mole fraction of 0.012, at $U_{\text{air}} = 0.7$ m/s and $T_{\text{air}} = 290$ K. Chemical kinetics are described by the ELTE syngas mechanism (Varga et al. 2016), comprising 14 species and 33 reactions.

3.2 Computational domain, parameters, grid, and boundary conditions

The cylindrical fuel injector, featuring inner and outer diameters $D = 4.58$ mm and $D_{out} = 6.34$ mm and length $L_{\text{inj}} = 6$ mm, is modelled through the Immersed Boundary Method (IBM). No-slip (viscous) wall boundary conditions are prescribed on the injector surfaces, a choice that proved critical for the accurate prediction of flame anchoring. The turbulent inflow described in Sec. 2.4 is applied on the injection patch: the power-law exponent n is chosen to be equal to 6.6 in accordance with previous studies of this configuration (Ciottoli et al. 2020), whereas the peak velocity $U_{\text{patch}} = 94.15$ m/s is selected so as to reproduce the experimental bulk velocity $U_{\text{bulk}} = 76$ m/s reported in Barlow et al. (2002). The value of the parameters related to the energy deposition in Eq. (4) and to the turbulent inflow described in Eq. (7) are reported in Table 1. The phases α_i and frequencies Ψ_i are drawn once, at initialization, from the uniform distributions also reported in Table 1; the inflow condition is nonetheless fully specified in the statistical sense.

The computational domain spans $L_x = 0.284$ m, $L_y = 0.183$ m, and $L_z = 0.183$ m in the streamwise and the two cross-stream directions, corresponding to $62D \times 40D \times 40D$. In the streamwise direction, the 62 diameters include the injector pipe (1.31D) and provide sufficient downstream extent to mitigate outflow effects. At $x = -0.006$ m the coflow conditions are imposed as inflow, whereas zero-gradient (Neumann) conditions are imposed at all the remaining boundaries; at the outflow, the zero-gradient condition is supplemented by a backflow suppression, setting the

Table 1 Energy deposition and turbulent inflow parameters: value and units

Quantity	Value	Units
A	$4 \cdot 10^7$	[W/(m^{3}K)]
r_{int}	0.00229	[m]
r_{ext}	0.00317	[m]
T_{obj}	1600	[K]
ϵ	10^4	[1/m]
x_{obj}	$1 \cdot 10^{-3}$	[m]
t_{obj}	10^{-4}	[s]
σ_x	$5 \cdot 10^6$	[1/m^2]
σ_t	$3 \cdot 10^8$	[1/s^2]
B_i	$0.5\, u'_{\mathrm{exp}}(x=0)$	[m/s]
α_i	rand[0,2π)	[rad]
Ψ_i	rand[0,10^5)	[rad/s]
n	6.6	[-]

wall-normal velocity to zero on boundary faces experiencing instantaneous inflow.
All statistics presented in Sec. 4 are collected at $x/D \leq 57.1$, upstream of the affected region; the acoustic velocity and temperature perturbations associated with the background pressure fluctuations measured in the quiescent coflow ($p'_{\mathrm{rms}} \approx 20$–$30$ Pa) are $u'_{\mathrm{ac,rms}} = p'_{\mathrm{rms}}/(\rho_\infty c_\infty) \lesssim 0.08$ m/s and $T'_{\mathrm{ac,rms}} \lesssim 0.1$ K, more than one and three orders of magnitude below the turbulent fluctuations at the measurement stations, respectively. A sketch of the computational domain is provided in Fig. 1. To resolve the whole range of spatial and temporal scales of the turbulent reacting flow without any subgrid-scale turbulence or combustion modelling, the domain is discretized with $n_x \times n_y \times n_z = 1680 \times 1428 \times 1428$ points, for a total of approximately 3.43 billion grid nodes. The grid is non-uniform, with points clustered near the injector exit and along the shear layers, and minimum spacings $\Delta x_{\mathrm{min}} = 100$ μm and $\Delta y_{\mathrm{min}} = \Delta z_{\mathrm{min}} = 74$ μm.

3.3 Grid resolution assessment

Since the solver is compressible, the Kolmogorov scale η is evaluated using the formulation introduced by Knaus and Pantano (2009), which accounts for density variations, and the local grid resolution is measured by the characteristic cell size $\Delta = (l_x l_y l_z)^{1/3}$. With the adopted resolution, 99.8% of the volume satisfies $\Delta/\eta \leq 2$ and 97.0% satisfies $\Delta/\eta \leq 1$ (97.1% and 88.5%, respectively, in terms of grid cells, the difference reflecting the mesh clustering in the near field, where the resolution requirements are most severe), as shown in Fig. 2.
It should be noted that the condition $\Delta \leq \eta$ is more restrictive than what is actually required for an accurate representation of the dissipative scales. The dissipation spectrum peaks at wavelengths of approximately 24η (Pope 2000) and its content becomes negligible beyond $\kappa\eta \approx 1.5$, so that a faithful DNS only requires the smallest resolved scale to be of the order of η, rather than η itself (Moin and Mahesh 1998). Accordingly, the established resolution criterion for simulations of homogeneous turbulence is $\kappa_{max}\eta \geq 1.5$, where $\kappa_{max} = \pi/\Delta$ is the highest resolved wavenumber, corresponding

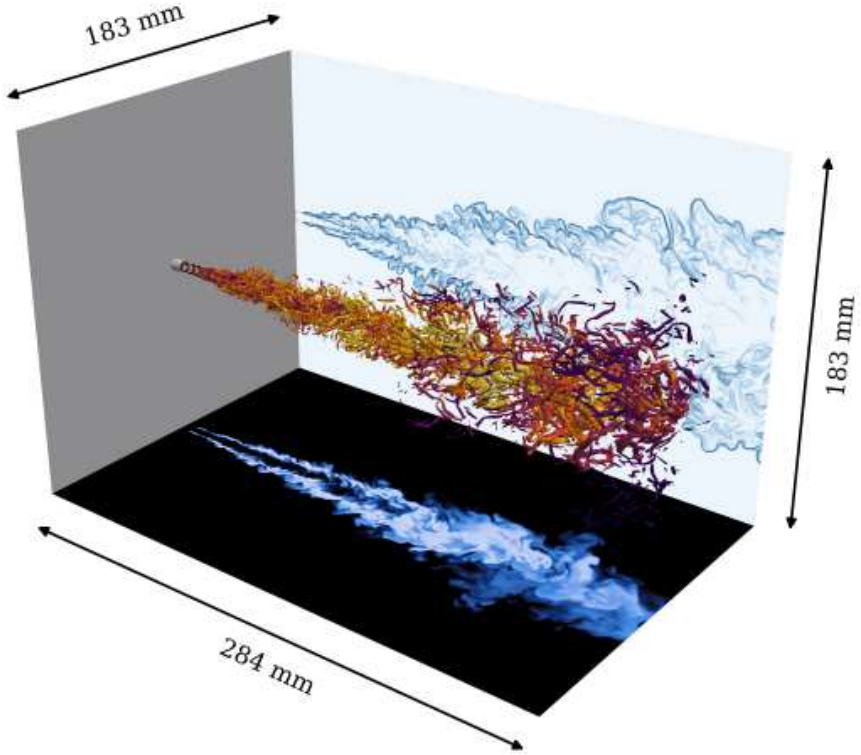


Fig. 1 Sketch of the computational domain employed in the simulation

to a grid spacing (Pope 2000; Yeung and Pope 1989)

$$\frac{\Delta}{\eta} \lesssim 2, \tag{8}$$

and grid spacings of a few Kolmogorov lengths are typical of DNS of turbulent free-shear flows (Moin and Mahesh 1998).
In the present simulation, the region where Δ/η exceeds 2 is confined to the pipe interior and to the near field, at $x/D \lesssim 13$ and $r/D \lesssim 0.7$, i.e. within and around the potential core. Particular attention is devoted to the initial shear layer, which governs the early jet development and the entrainment of ambient fluid. Within the annulus bounded by the inner and outer nozzle lip radii ($0.5 \leq r/D \leq 0.69$) and extending up to $x/D = 5$, the resolution ratio attains a mean value of $\Delta/\eta = 1.25$, with a localized peak of $\Delta/\eta = 2.2$ at $x/D \approx 1.7$, where transition of the annular shear layer takes place and the dissipation rate is highest; fewer than 0.5% of the grid points in this region exceed $\Delta/\eta = 2$. The resolution of the initial shear layer is therefore consistent with the criterion of Eq. (8), with only a marginal and highly localized exceedance.
In addition to the Kolmogorov-scale assessment, the resolution of the flame structure is verified. Unlike a premixed flame, a diffusion flame has no intrinsic thickness (Poinsot

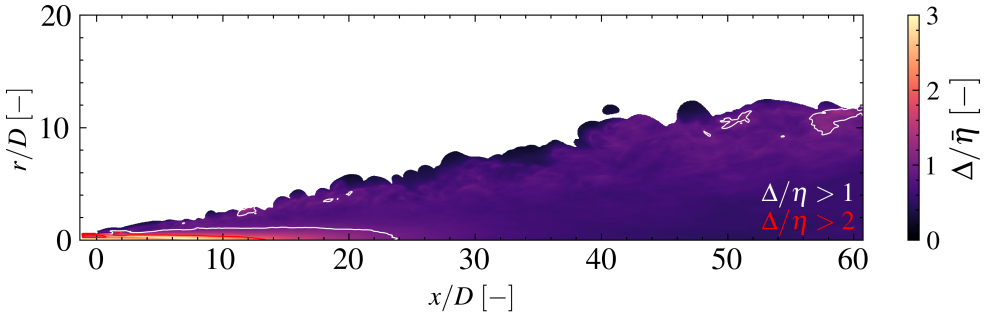


Fig. 2 Kolmogorov resolution 2D map. The white contour encloses the region with $\Delta/\eta > 1$, the red contour the region with $\Delta/\eta > 2$

and Veynante 2011; Peters 2000), since the width of its layers depends on the local scalar dissipation rate. In DNS of non-premixed flames the grid is therefore required to resolve the thinnest reaction zones (Domingo and Vervisch 2023), and its adequacy is commonly expressed as the number of grid points across the radical layers, typically the OH layer, about ten points being the usual target (Pantano 2004; Lignell et al. 2008; Attili et al. 2014). The OH layer is therefore considered here, its thickness δ_{OH} being defined as the full width at half maximum of the Y_{OH} profile.

This thickness is obtained from a library of steady counterflow diffusion flames computed with Cantera (Goodwin et al. 2025) and with the same kinetic mechanism and conditions (i.e. temperature, pressure, composition) of the DNS. The library is built with the continuation procedure of Fiala and Sattelmayer (2014) along the burning branch, from the low-strain limit up to extinction, and each flame is identified by the scalar dissipation rate at the stoichiometric mixture fraction, χ_{st}, where $\chi = 2\alpha|\nabla Z|^2$, Z is the Bilger mixture fraction (Bilger et al. 1990) and α the thermal diffusivity.

The flame resolution is evaluated on an instantaneous DNS field, on the grid points lying on the stoichiometric surface ($|Z - Z_{st}| \leq 0.05$, with $Z_{st} = 0.295$, and $\chi > 1\ \mathrm{s}^{-1}$). At each point, the local scalar dissipation rate is used to read δ_{OH} from the library, and the number of grid points across the layer is computed as $N_{OH} = \delta_{OH}/\Delta$, where $\Delta = (l_x l_y l_z)^{1/3}$ is the same aforementioned characteristic cell size.

The results are consistent with the Kolmogorov-scale assessment: the OH layer is described by at least 10 points for 82% of the samples and by at least 5 points for 97% of them. The samples with $N_{OH} < 4$ are 1.5% of the total: they are found in the jet shear layer ($0.5 \lesssim r/D \lesssim 2$), and most of them are located at $x/D < 17$, i.e. upstream of the first experimental measurement station. The median resolution is $N_{OH} = 20$. The lowest resolution is observed in the near field ($x/D < 8$, 4% of the samples), where the high dissipation rates of the initial shear layer reduce the median value to $N_{OH} = 6$. In the region $x/D \geq 17$, where the comparison with the experimental data is carried out and which contains 84% of the samples, the median value is $N_{OH} = 22$; the OH layer is described by at least 10 points for 88% of the samples and by at least 5 points for 99% of them. The flame is therefore well resolved in the region of interest, the resolution being marginal only in the near field. Fig. 3 shows the map of N_{OH}.

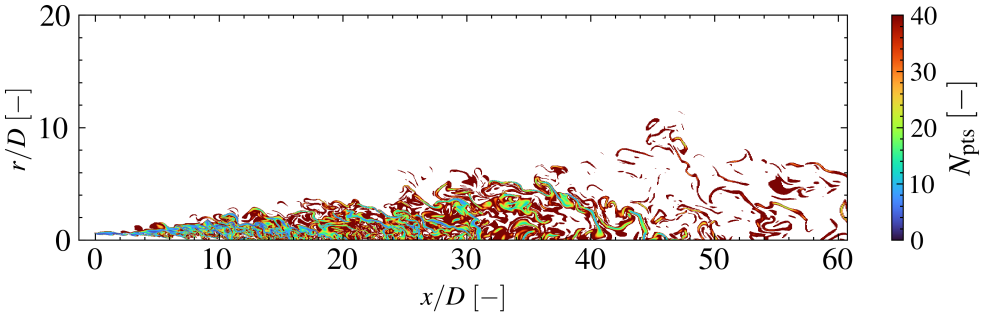


Fig. 3 Number of points across the OH thickness N_{OH}, 2D map

4 Results

Time integration is performed with a Courant–Friedrichs–Lewy (CFL) number of 0.65, yielding a time step of $\Delta t \approx 5 \times 10^{-8}$ s for a total physical simulation time of $t = 0.1$ s. Based on the flow-through time, defined as FTT $= L_x/U_{\text{bulk}} \approx 3.7$ ms, the total integration window spans approximately 27 FTT. To ensure that turbulence statistics are accumulated in a statistically stationary state, the first 10 FTT are discarded as an initial transient period, leaving a window of 17 FTT for data collection.

For the radial and conditional mean analysis, the flow fields were sampled on two orthogonal centerplanes (XY and XZ) passing through the injector axis. Exploiting the statistical axisymmetry of the configuration, each centerplane was split at the jet axis into two semi-planes, yielding four azimuthal samples ($\theta = 0°$, $90°$, $180°$, $270°$) that were averaged together.

The computation was carried out on 398 NVIDIA A100 SXM4 64 GB GPUs, with a wall-clock time of approximately 2 s per time step and a total runtime of about 45 days.

A snapshot of the instantaneous temperature field is shown in Fig. 4, illustrating the transition of the jet, the development of the shear-layer instabilities, and the attached flame anchored at the injector post-tip.

4.1 Centerline statistics

The comparison with the experimental data is first carried out along the jet centerline. Figure 5 shows mean and RMS profiles of temperature T, Bilger mixture fraction Z, the three velocity components U, V, W, and the mass fractions of seven measured species. The DNS reproduces the shape of all measured profiles, but the curves are systematically displaced in the axial direction: the numerical flame develops closer to the injector than the experimental one. The displacement S is quantified by least-squares fitting, minimizing

$$E(S) = \sum_i \left[q_{\text{DNS}}(x_i - S) - q_{\text{exp}}(x_i)\right]^2 \tag{9}$$

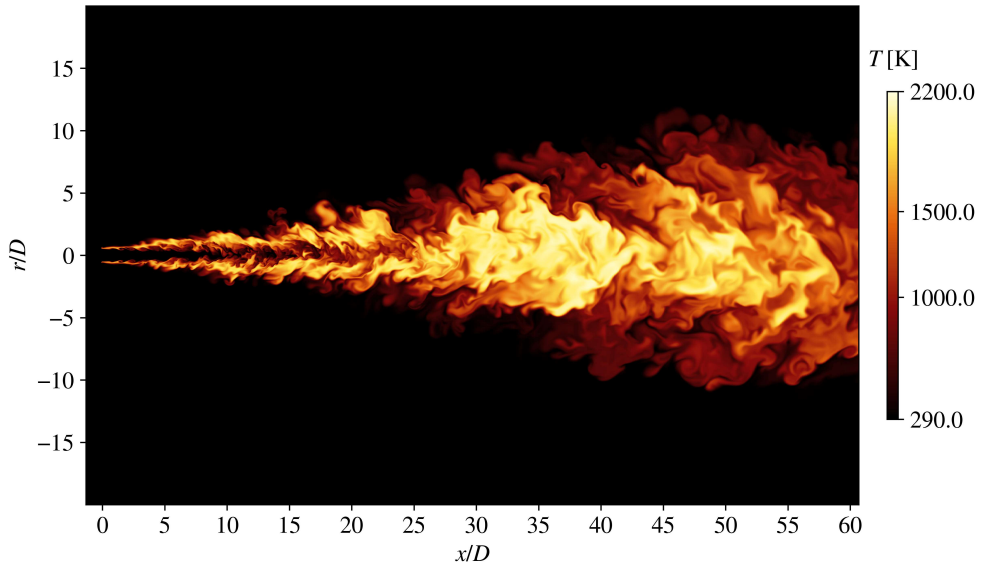
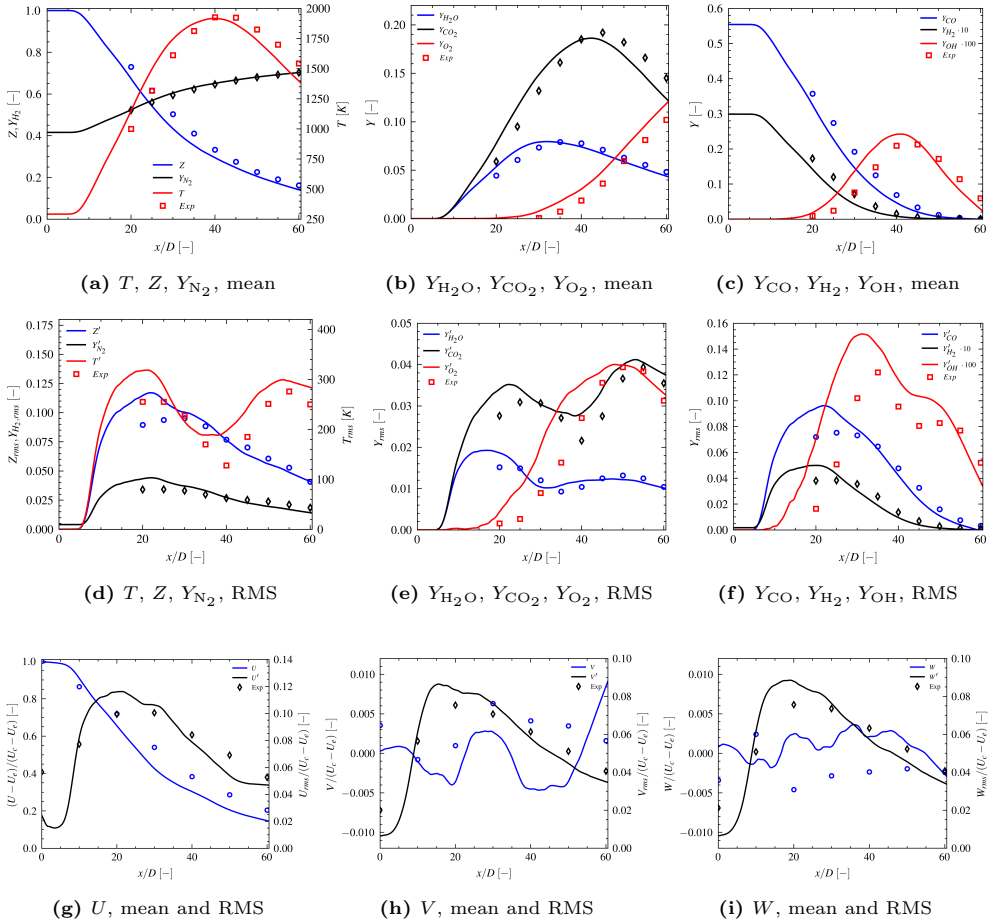


Fig. 4 Snapshot of the instantaneous temperature field for flame A

over the experimental stations $20 \leq x_i/D \leq 60$, well downstream of the potential core. The fit is repeated independently for the seven measured mean quantities q, and the results are collected in Table 2. These quantities are the conserved scalar Z, the temperature, and five reactive species; the seven fits return mutually consistent values, with mean $S = 2.91D$ (13.3 mm): the quantity-to-quantity scatter, $0.26D$, is comparable to the individual fit uncertainties, supporting a single common shift. In particular, no systematic separation emerges between the conserved scalar and the reactive species: the largest deviations from the mean, for Y_{O_2} and Y_{CO}, are of opposite sign and remain within two standard deviations from the mean. The consistency of S across conserved and reactive quantities indicates that the discrepancy is a rigid translation of the jet development rather than an artefact of the chemical or transport modelling, which would displace the reactive scalars differently from the conserved ones. Plotting the mean quantities against Z leads to the same conclusion: when temperature and species mass fractions are plotted against the mixture fraction, a representation invariant under any axial shift, the DNS and the measurements collapse (Fig. 6). Over the stations at $20 \leq x/D \leq 60$, each experimental measurement is compared with the DNS curve at the same measured value of Z, without any axial shift: the deviations are at most 1.2% in T, 2.6% in Y_{H_2O} and 5.1% in Y_{CO}, relative to the measured values; at the leanest station ($x/D = 60$) the measured Y_{CO} falls below 10^{-3} and a relative measure loses meaning, but its absolute deviation from the DNS curve remains within 4×10^{-4}. The entire discrepancy observed in physical space is thus carried by the mixture-fraction field, that is, by the jet hydrodynamics.



(a) T, Z, $Y_{\mathrm{N_2}}$, mean **(b)** $Y_{\mathrm{H_2O}}$, $Y_{\mathrm{CO_2}}$, $Y_{\mathrm{O_2}}$, mean **(c)** Y_{CO}, $Y_{\mathrm{H_2}}$, Y_{OH}, mean

(d) T, Z, $Y_{\mathrm{N_2}}$, RMS **(e)** $Y_{\mathrm{H_2O}}$, $Y_{\mathrm{CO_2}}$, $Y_{\mathrm{O_2}}$, RMS **(f)** Y_{CO}, $Y_{\mathrm{H_2}}$, Y_{OH}, RMS

(g) U, mean and RMS **(h)** V, mean and RMS **(i)** W, mean and RMS

Fig. 5 Comparison between DNS results (solid lines) and experimental data (symbols) along the jet centerline

Figures 7 and 8 compare the original and shifted centerline profiles with the measurements: plotted against x, the DNS profiles show markedly better agreement with the experimental data.

This shift is likely attributable to the inflow conditions, which are only partially documented in the experimental dataset (Barlow et al. 2002). The LDV survey reports a maximum mean exit velocity $U_{\max} = 104.88$ m/s, which the reference LES study (Ciottoli et al. 2020) matched by prescribing $U_{\mathrm{patch}} = 105.4$ m/s. The measured exit profile, however, appears to be internally inconsistent: its integral corresponds to a bulk velocity of about 81 m/s, $\sim 7\%$ above the declared value $U_{\mathrm{bulk}} = 76$ m/s. The origin of this inconsistency cannot be established from the available documentation. A plausible contribution is heating of the fuel pipe: since the flame is anchored at the burner lip, the duct wall temperature rises above ambient, reducing the gas density

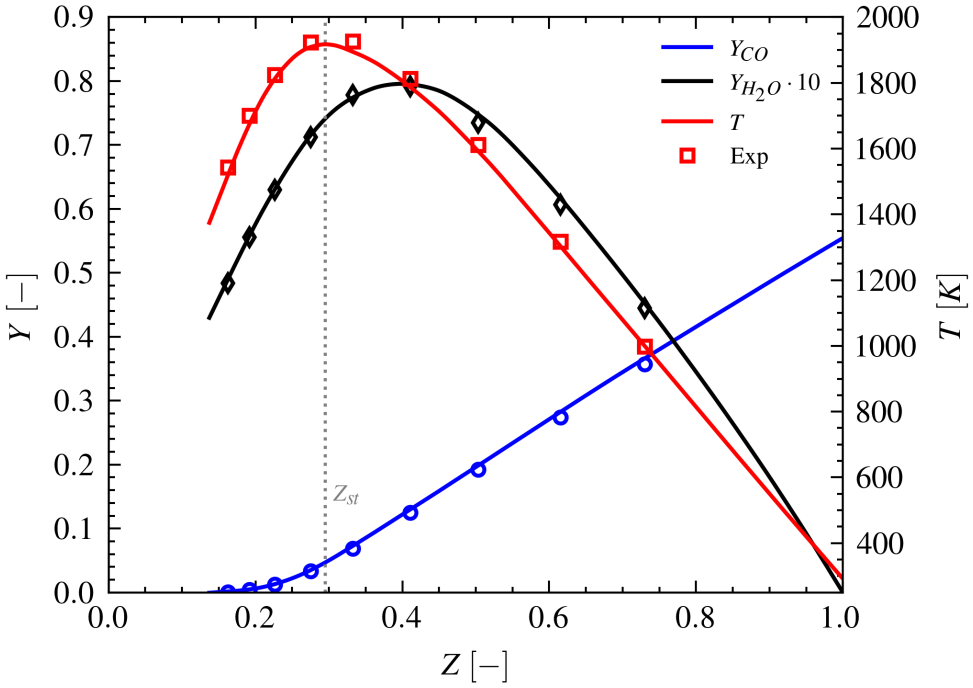


Fig. 6 Y_{CO} and $Y_{\mathrm{H_2O}}$ on the left axis, T on the right axis plotted against the mixture fraction Z. DNS results in solid lines, experimental data represented by markers, and $Z_{\mathrm{st}} = 0.295$ shown as a dotted line

Table 2 Axial shift S obtained independently for each measured centerline quantity by minimizing Eq. (9) over $20 \leq x_i/D \leq 60$. Uncertainties are one standard deviation, estimated from the curvature of $E(S)$ at the minimum

Quantity	S/D	S [mm]
Z	2.91 ± 0.23	13.3
T	2.78 ± 0.23	12.7
Y_{CO}	2.42 ± 0.26	11.1
$Y_{\mathrm{H_2O}}$	2.90 ± 0.26	13.3
$Y_{\mathrm{CO_2}}$	2.99 ± 0.25	13.7
$Y_{\mathrm{O_2}}$	3.23 ± 0.21	14.8
$Y_{\mathrm{H_2}}$	3.11 ± 0.22	14.2
Mean	2.91	13.3

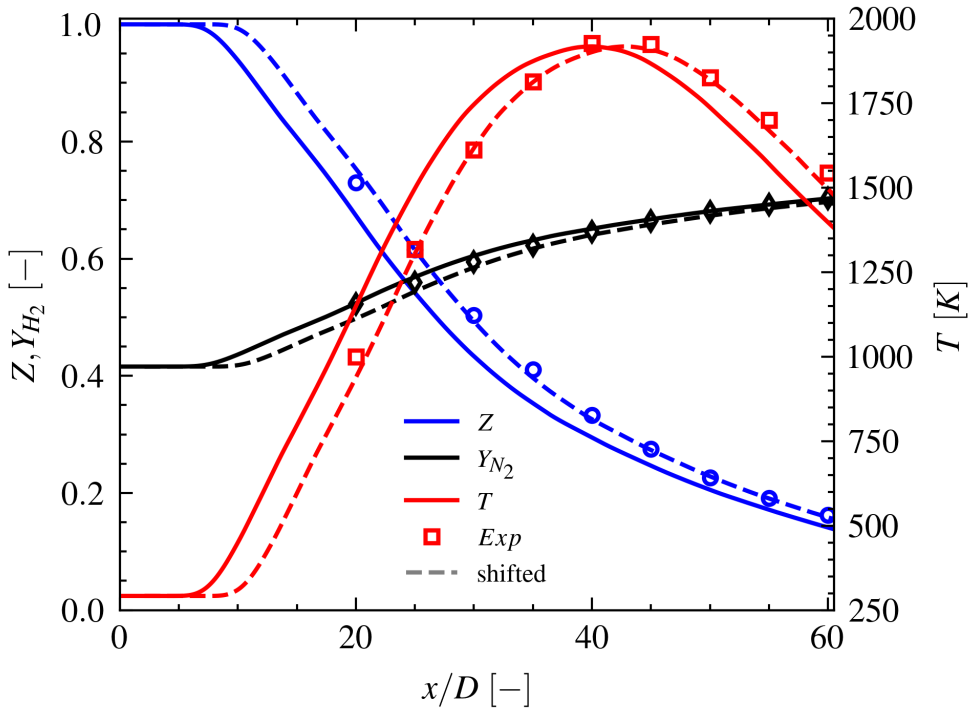


Fig. 7 Centerline profiles of T, Z, and Y_{N_2}: shifted DNS curves (dashed lines), non-shifted DNS curves (solid lines), and experimental data (symbols)

near the exit and increasing, at fixed mass flow rate, the velocity measured by LDV. No wall or exit gas temperature measurements are reported, however, so this explanation cannot be confirmed.

The present simulation matches the bulk velocity and the declared mass flow rate instead, prescribing a power-law profile (see Eq. (5)) with peak velocity $U_{\text{patch}} = 94.15$ m/s. This condition is verified a posteriori: the time-averaged volume flux realized in our simulation is $q_{\text{DNS}} = 1.248 \times 10^{-3}$ m^3/s, and the averaged bulk velocity is $U_{\text{bulk}} = 75.74$ m/s, while the experimental declared values are $q_{\text{exp}} = 1.252 \times 10^{-3}$ m^3/s and $U_{\text{bulk}} = 76$ m/s. Furthermore, the DNS time-averaged Reynolds number is equal to $Re = 16944$, against a declared value of $Re = 16700$, with the residual difference reflecting the mixture viscosity of the adopted transport model.

Matching the mass flux also constrains the exit momentum flux. At a given mass flux, the momentum flux is $M = \dot{m}\, U_{\text{bulk}}\, K$, where K is the momentum-flux correction factor of the exit profile (White 2011)

$$K = \frac{1}{A U_{\text{bulk}}^2} \int_A u^2(r) dA, \tag{10}$$

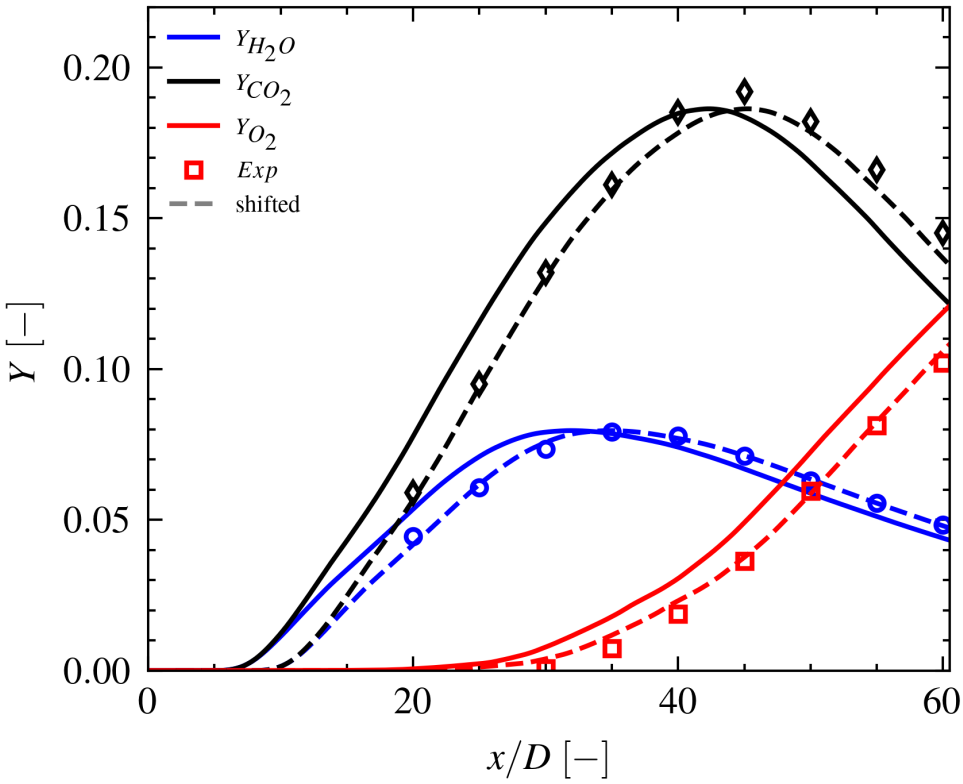


Fig. 8 Centerline profiles of $Y_{\mathrm{H_2O}}$, $Y_{\mathrm{CO_2}}$, and $Y_{\mathrm{O_2}}$: shifted DNS curves (dashed lines), non-shifted DNS curves (solid lines), and experimental data (symbols)

and is $K = 1.023$ for the prescribed power-law and 1.09 for the integrated LDV profile. Including the $\approx 0.3\%$ mass-flux deficit measured in the DNS, the momentum flux of the simulated jet matches the experimental one to within 7%:

$$\frac{M_{\mathrm{DNS}}}{M_{\mathrm{exp}}} = \left(\frac{q_{\mathrm{DNS}}}{q_{\mathrm{exp}}}\right)^2 \cdot \frac{K_{\mathrm{pl}}}{K_{\mathrm{LDV}}} = 0.93. \tag{11}$$

Classical similarity arguments (Thring and Newby 1953; George 1989) indicate that jets sharing the exit fluxes of mass and momentum develop identical far fields up to a virtual-origin displacement, and experiments on jets with matched momentum but different exit profiles and turbulence levels report displacements of one to a few diameters with decay constants changing by only a few percent (Mi et al. 2001; Xu and Antonia 2002). The fitted $S = 2.91D$ is consistent with this picture: the simulated jet carries a momentum flux about 7% lower than the experimental one, and its near field further differs from the experiment in exit profile shape and turbulence level, both of which are known to shift the virtual origin by one to a few diameters. The combined effect displaces the axial development towards the injector while leaving the far-field

essentially unchanged.
However, a direct sensitivity study of the axial shift to the inflow specification would require repeating the present computation for at least one alternative inflow condition, and is beyond the available computational resources. An indirect assessment is nonetheless provided by the reference LES of this configuration (Ciottoli et al. 2020), which employed the same analytical inflow family, but employed a higher peak velocity, as mentioned above. For this profile shape, that choice corresponds to a bulk velocity of approximately $U_{\mathrm{bulk}} = 85$ m/s. The LES reproduced the measured axial development with no appreciable displacement, while the present DNS, prescribing the same profile shape at the lower, declared flux, develops closer to the injector. The two computations also differ in combustion closure, numerical schemes, and resolution, so this comparison cannot be regarded as a controlled single-parameter study; nevertheless, the axial placement of the flame follows the prescribed inflow flux in the direction predicted by the integral argument above. This observation, combined with the consistency of S across conserved and reactive scalars and with the collapse of the state relations discussed above, supports attributing the shift to the residual uncertainty in the inflow specification rather than to the chemical or transport modelling.

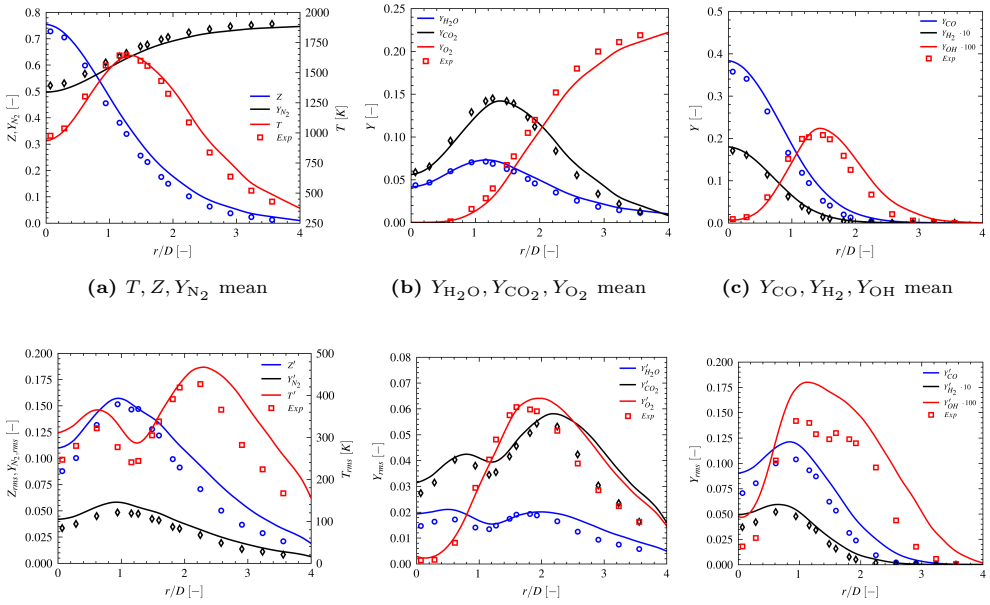
4.2 Radial profiles

Radial profiles of the measured quantities are available at the experimental stations $x/D = 20, 30, 40, 50$, and 60. To ensure a consistent comparison, the experimental data are compared with the DNS results extracted at the corresponding shifted locations. This means, for example, that measured values at $x/D = 20$ are compared with the results at $x/D = 17.09$, where x is the DNS axial coordinate, with $x = 0$ at the pipe outlet section. As a consequence, the pipe inlet section is located at $x/D = -L_{inj}/D = -1.31$. The comparison is thus performed at the DNS stations $x/D = 17.09, ..., 57.09$. In addition, DNS statistics are collected at every diameter from $x/D = 10$ to $x/D = 60$ in the unshifted simulation frame; the complete dataset is provided as Supplementary Material, to ensure full reproducibility of this numerical benchmark. For brevity, the comparison is shown here only for the stations $x/D = 20$ and 50, in Figs. 9 and 10.

When the comparison is carried out at the equivalent experimental coordinate, excellent agreement between numerical and experimental data is achieved for both mean and RMS profiles of all the measured quantities.

4.3 Conditional statistics

The agreement improves further when the statistics are conditioned on the Bilger mixture fraction Z. Conditional means are again available at every station from $x/D = 10$ to $x/D = 60$ in the Supplementary Material; representative results at $x/D = 20$ and 50 are reported in Figs. 11-14, again compared with equivalent shifted coordinates $x/D = 17.09$ and $x/D = 47.09$.
As shown in Fig. 11, the conditional mean temperature closely follows the experimental data and, as expected, peaks at mixture fraction values slightly richer than the stoichiometric value $Z_{\mathrm{st}} = 0.295$.
Most species exhibit excellent agreement at all locations as well, as illustrated in



(a) $T, Z, Y_{\mathrm{N_2}}$ mean **(b)** $Y_{\mathrm{H_2O}}, Y_{\mathrm{CO_2}}, Y_{\mathrm{O_2}}$ mean **(c)** $Y_{\mathrm{CO}}, Y_{\mathrm{H_2}}, Y_{\mathrm{OH}}$ mean

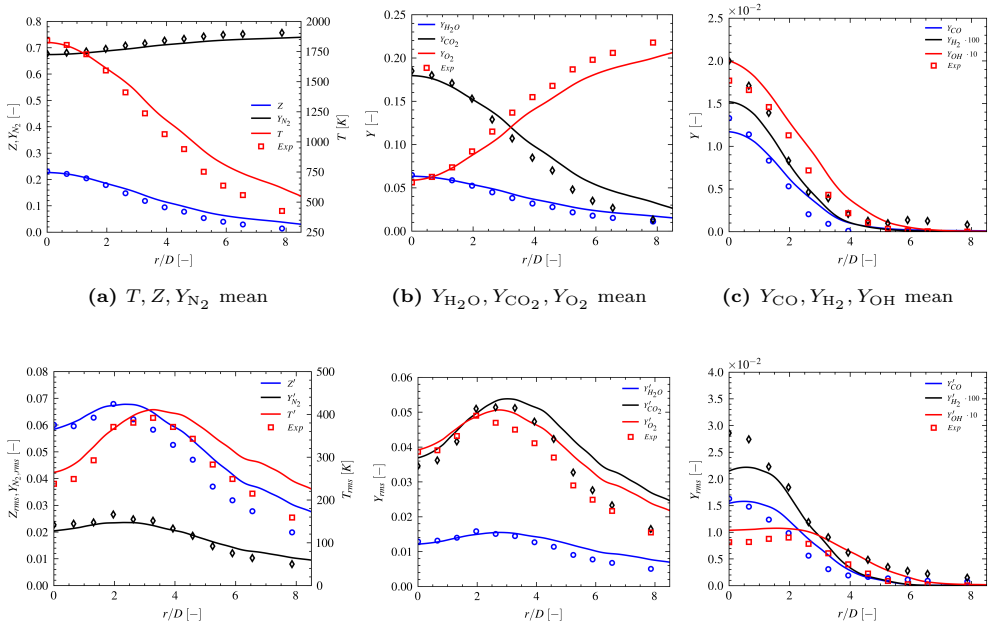
(d) $T, Z, Y_{\mathrm{N_2}}$ rms **(e)** $Y_{\mathrm{H_2O}}, Y_{\mathrm{CO_2}}, Y_{\mathrm{O_2}}$ rms **(f)** $Y_{\mathrm{CO}}, Y_{\mathrm{H_2}}, Y_{\mathrm{OH}}$ rms

Fig. 9 Comparison between results at $x/D = 17.09$ and experimental data at $x/D = 20$: DNS results (solid lines), experimental data (symbols)

Figs. 12 and 13 for CO_2 and H_2. Only the OH mass fraction exhibits appreciable discrepancies, with the peak value being overpredicted by approximately 25% across all measurement stations, as shown in Fig. 14. This consistency suggests a systematic bias, either in the OH measurement calibration or inherited from the kinetic mechanism, rather than a spatially evolving model deficiency.
Overall, the agreement obtained for temporal means, RMS fluctuations, and conditional means (once the axial shift induced by the inflow specification is accounted for) supports the reliability of the present simulation, and the resolution and extent of the collected database qualify this work as a fully documented and reproducible numerical benchmark.

5 Conclusions

In this work, the direct numerical simulation of the Sandia/ETH-Zurich $CO/H_2/N_2$ flame A was presented, performed with the GPU-accelerated solver STREAmS-2.0 on a grid of approximately 3.43 billion points, with detailed chemistry and mixture-averaged molecular transport.
Since the experimental jet inlet velocity profile is not documented, an analytical power-law profile with superimposed synthetic perturbations was prescribed, with parameters chosen to match the declared experimental bulk velocity. The results exhibit a systematic axial shift of $S \approx 2.91D$ with respect to the measurements, which is attributed



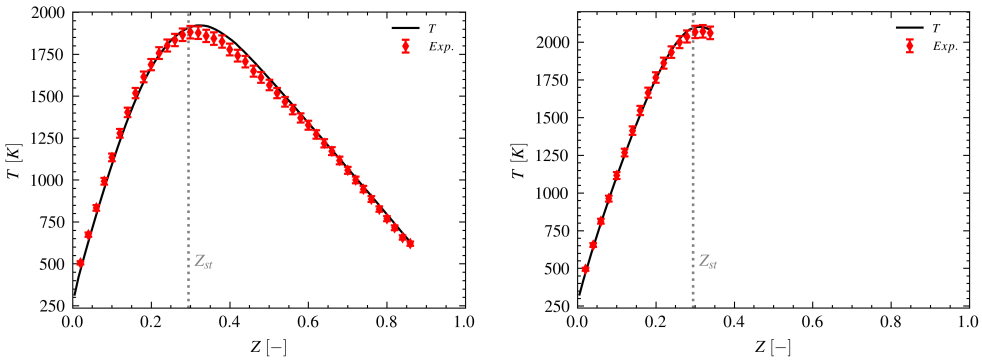
(a) $T, Z, Y_{\mathrm{N_2}}$ mean **(b)** $Y_{\mathrm{H_2O}}, Y_{\mathrm{CO_2}}, Y_{\mathrm{O_2}}$ mean **(c)** $Y_{\mathrm{CO}}, Y_{\mathrm{H_2}}, Y_{\mathrm{OH}}$ mean

(d) $T, Z, Y_{\mathrm{N_2}}$ rms **(e)** $Y_{\mathrm{H_2O}}, Y_{\mathrm{CO_2}}, Y_{\mathrm{O_2}}$ rms **(f)** $Y_{\mathrm{CO}}, Y_{\mathrm{H_2}}, Y_{\mathrm{OH}}$ rms

Fig. 10 Comparison between results at $x/D = 47.09$ and experimental data at $x/D = 50$: DNS results (solid lines), experimental data (symbols)

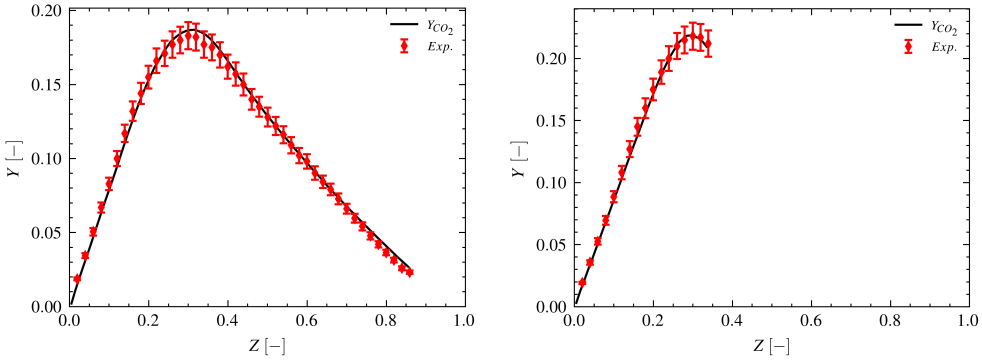
to the residual uncertainty in the inflow specification. Once this shift is accounted for, the simulation reproduces the experimental database with excellent accuracy, in terms of mean and RMS profiles along the centerline, mean and RMS radial profiles at all measurement stations, and means conditioned on the Bilger mixture fraction; only the conditional OH mass fraction displays appreciable deviations, compatible with a systematic bias in either the measurement calibration or the kinetic mechanism.

Since every feature of the numerical setup is analytical and fully documented, the present simulation constitutes a well-defined benchmark for the validation of reacting-flow solvers and combustion models. To this end, the complete statistical database is made available at every diameter between $x/D = 10$ and $x/D = 60$, guaranteeing full reproducibility in the statistical sense: the deterministic parameters are documented in full, and the stochastic inflow phases are drawn from prescribed distributions. Furthermore, to the best of the authors' knowledge, the present computation, covering a laboratory-scale domain of $28.4 \times 18.3 \times 18.3$ cm^3, considerably larger than the centimeter-scale domains typically employed in state-of-the-art reacting DNS (Minamoto and Chen 2016; Coulon et al. 2023; Scialabba et al. 2025), represents one of the largest DNS of a turbulent reacting flow performed to date. The fact that it was completed in about 45 days on 398 GPUs demonstrates that, by leveraging modern GPU-based HPC architectures, high-fidelity simulations of laboratory-scale flames are now within reach.



(a) $x_{\mathrm{exp}}/D = 20$ vs $x_{\mathrm{DNS}}/D = 17.09$ **(b)** $x_{\mathrm{exp}}/D = 50$ vs $x_{\mathrm{DNS}}/D = 47.09$

Fig. 11 Conditional mean of temperature on the Bilger mixture fraction Z: DNS results (solid lines) and experimental data (symbols, with systematic uncertainty bars)

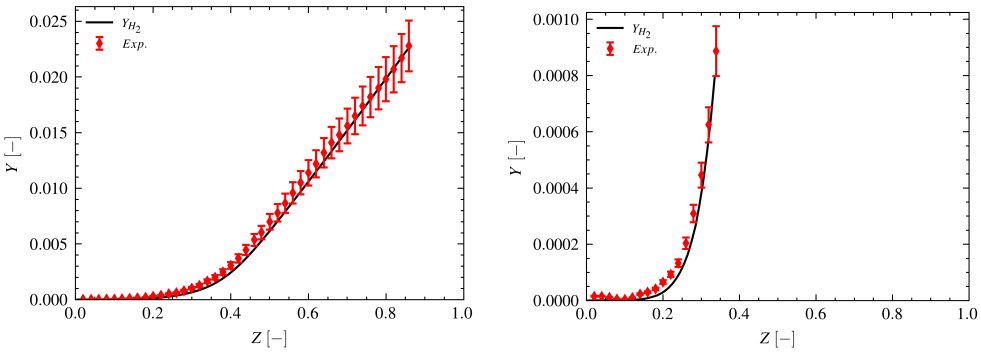


(a) $x_{\mathrm{exp}}/D = 20$ vs $x_{\mathrm{DNS}}/D = 17.09$ **(b)** $x_{\mathrm{exp}}/D = 50$ vs $x_{\mathrm{DNS}}/D = 47.09$

Fig. 12 Conditional mean of $Y_{\mathrm{CO_2}}$ on the Bilger mixture fraction Z: DNS results (solid lines) and experimental data (symbols, with systematic uncertainty bars)

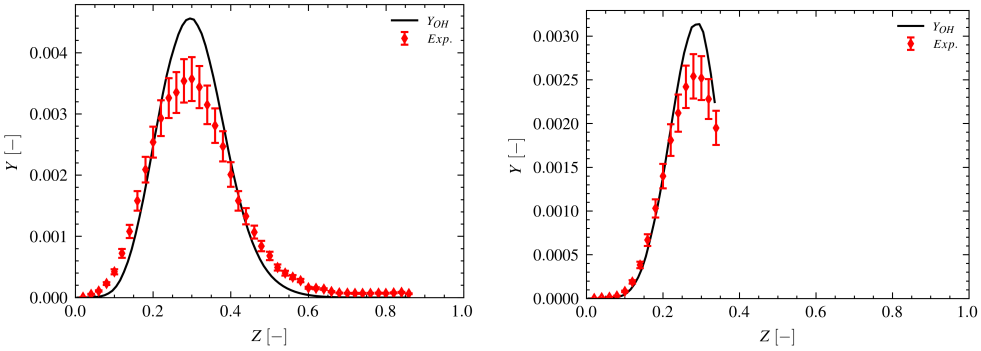
Declarations

Acknowledgements. The authors gratefully acknowledge the financial support provided by the European Space Agency (ESA) under the Technical Support Activities for the STS PNRR Project (PNRR CUP J58G21000020007).
The view expressed herein can in no way be taken to reflect the official opinion of the European Space Agency, the Presidency of the Council of Ministers of the Italian Republic, and the European Commission. Views and opinions expressed are those of the author(s) only, and the European Union/European Commission/ESA/Presidency of Council of Ministers of the Italian Republic cannot be held responsible for any use which may be made of the information contained therein.



(a) $x_{\mathrm{exp}}/D = 20$ vs $x_{\mathrm{DNS}}/D = 17.09$ **(b)** $x_{\mathrm{exp}}/D = 50$ vs $x_{\mathrm{DNS}}/D = 47.09$

Fig. 13 Conditional mean of $Y_{\mathrm{H_2}}$ on the Bilger mixture fraction Z: DNS results (solid lines) and experimental data (symbols, with systematic uncertainty bars)



(a) $x_{\mathrm{exp}}/D = 20$ vs $x_{\mathrm{DNS}}/D = 17.09$ **(b)** $x_{\mathrm{exp}}/D = 50$ vs $x_{\mathrm{DNS}}/D = 47.09$

Fig. 14 Conditional mean of Y_{OH} on the Bilger mixture fraction Z: DNS results (solid lines) and experimental data (symbols, with systematic uncertainty bars)

Authors' contribution. **E. F:** Conceptualization, Methodology, Software, Investigation, Visualization, and Writing - original draft. **A. N:** Project administration, Conceptualization, Funding acquisition. **M. V:** Project administration, Conceptualization, Supervision, Funding acquisition. **M. B:** Conceptualization, Software, Resources, Writing - review & editing. **P.P. C:** Conceptualization, Supervision, Writing - review & editing. All authors read and approved the final manuscript.

Funding. Funded by the European Union - NextGenerationEU and by the Presidency of the Council of Ministers pursuant to Article 1, paragraph 254, of Law 160/2019 and by the Presidency of the Council of Ministers from the Complementary Fund.

Data availability. The data used to perform the analysis and generate the figures, including the datasets at all axial stations, are provided as Supplementary Material accompanying this manuscript. Additional data are available from the corresponding author upon reasonable request.

References

ANSYS: Chemkin Theory Manual 17.0 (15151). Reaction Design: San Diego (2015)

Attili, A., Bisetti, F., Mueller, M.E., Pitsch, H.: Formation, growth, and transport of soot in a three-dimensional turbulent non-premixed jet flame. Combustion and Flame **161** (2014) https://doi.org/10.1016/j.combustflame.2014.01.008

Barlow, R.S., Fiechtner, G.J., Carter, C.D., Flury, M.: Sandia/ETH-Zurich $CO/H_2/N_2$ Flame Data — Release 1.1. International Workshop on Measurement and Computation of Turbulent Nonpremixed Flames (TNF), Sandia National Laboratories, Livermore, CA. Accessed September 2026 (2002). https://tnfworkshop.org/data-archives/

Barlow, R.S., Fiechtner, G.J., Carter, C.D., Chen, J.-Y.: Experiments on the scalar structure of turbulent $CO/H_2/N_2$ jet flames. Combustion and Flame **120** (2000) https://doi.org/10.1016/S0010-2180(99)00126-1

Bernardini, M., Modesti, D., Salvadore, F., Pirozzoli, S.: Streams: A high-fidelity accelerated solver for direct numerical simulation of compressible turbulent flows. Computer Physics Communications **263**, 107906 (2021) https://doi.org/10.1016/j.cpc.2021.107906

Bernardini, M., Modesti, D., Salvadore, F., Sathyanarayana, S., Della Posta, G., Pirozzoli, S.: Streams-2.0: Supersonic turbulent accelerated navier-stokes solver version 2.0. Computer Physics Communications **285**, 108644 (2023) https://doi.org/10.1016/j.cpc.2022.108644

Bilger, R.W., Stårner, S.H., Kee, R.J.: On reduced mechanisms for methane–air combustion in nonpremixed flames. Combustion and Flame **80** (1990) https://doi.org/10.1016/0010-2180(90)90122-8

Chen, J.H.: Petascale direct numerical simulation of turbulent combustion — fundamental insights towards predictive models. Proceedings of the Combustion Institute **33**(1), 99–123 (2011) https://doi.org/10.1016/j.proci.2010.09.012

Ciottoli, P.P., Lee, B.J., Lapenna, P.E., Galassi, R.M., Hernández-Pérez, F.E., Martelli, E., Valorani, M., Im, H.G.: Large eddy simulation on the effects of pressure on syngas/air turbulent nonpremixed jet flames. Combustion Science and Technology **192**(10), 1963–1996 (2020) https://doi.org/10.1080/00102202.2019.1632300

Coulon, V., Gaucherand, J., Xing, V., Laera, D., Lapeyre, C., Poinsot, T.: Direct numerical simulations of methane, ammonia-hydrogen and hydrogen turbulent premixed flames. Combustion and Flame **256** (2023) https://doi.org/10.1016/j.combustflame.2023.112933

Frahan, M.T.H., Rood, J.S., Day, M.S., Sitaraman, H., Yellapantula, S., Perry, B.A., Grout, R.W., Almgren, A., Zhang, W., Bell, J.B., Chen, J.H.: Pelec: An adaptive mesh refinement solver for compressible reacting flows. The International Journal of High Performance Computing Applications **37** (2023) https://doi.org/10.1177/10943420221121151

Domingo, P., Vervisch, L.: Recent developments in dns of turbulent combustion. Proceedings of the Combustion Institute **39** (2023) https://doi.org/10.1016/j.proci.2022.06.030

Fiala, T., Sattelmayer, T.: Nonpremixed counterflow flames: scaling rules for batch simulations. Journal of Combustion (2014) https://doi.org/10.1155/2014/484372

Forti, E., Bernardini, M., Stella, F., Valorani, M., Ciottoli, P.P.: Development and validation of a compressible multicomponent reactive flow solver based on streams-2.0. 11th EUROPEAN CONFERENCE FOR AEROSPACE SCIENCES (EUCASS) (2025)

Gadde, S., Wu, J., Gulati, A., McQuiggan, G., Koestlin, B., Prade, B.: Syngas Capable Combustion Systems Development for Advanced Gas Turbines, vol. 4: Cycle Innovations; Electric Power; Industrial and Cogeneration; Manufacturing Materials and Metallurgy (2006). https://doi.org/10.1115/GT2006-90970

Gargiulo, G., Ciottoli, P.P., Martelli, E., Malpica Galassi, R., Valorani, M.: Numerical analysis of laser-pulse transient ignition of oxygen/methane mixtures in rocket-like combustion chamber. Acta Astronautica **159** (2019) https://doi.org/10.1016/j.actaastro.2019.03.049

George, W.K.: The self-preservation of turbulent flows and its relation to initial conditions and coherent structures. In: George, W.K., Arndt, R. (eds.) Advances in Turbulence. Hemisphere (1989)

Ghenai, C.: Combustion of syngas fuel in gas turbine can combustor. Advances in Mechanical Engineering **2** (2010) https://doi.org/10.1155/2010/342357

Giacomazzi, E., Picchia, F.R., Arcidiacono, N., Cecere, D., Donato, F., Favini, B.: Unsteady simulation of a $CO/H_2/N_2$/air turbulent non-premixed flame. Combustion Theory and Modelling **12** (2008) https://doi.org/10.1080/13647830802276131

Gilbert, R.G., Luther, K., Troe, J.: Theory of thermal unimolecular reactions in the fall-off range. ii. weak collision rate constants. Berichte der Bunsengesellschaft fur physikalische Chemie **87** (1983) https://doi.org/10.1002/bbpc.19830870218

Goodwin, D.G., Moffat, H.K., Schoegl, I., Speth, R.L., Weber, B.W.: Cantera: An object-oriented software toolkit for chemical kinetics, thermodynamics, and transport processes (2025) https://doi.org/10.5281/zenodo.17620923

Gupta, K.K., Rehman, A., Sarviya, R.M.: Bio-fuels for the gas turbine: A review. Renewable and Sustainable Energy Reviews **14** (2010) https://doi.org/10.1016/j.rser.2010.07.025

Hirschfelder, J.O., Curtiss, C.F., Bird, R.B.: Molecular Theory of Gases and Liquids. John Wiley & Sons (1954)

Jiang, G.-S., Shu, C.-W.: Efficient implementation of weighted eno schemes. Journal of Computational Physics **126**(1), 202–228 (1996) https://doi.org/10.1006/jcph.1996.0130

Kerkemeier, S., Frouzakis, C.E., Tomboulides, A.G., Fischer, P., Bode, M.: nekCRF: A next generation high-order reactive low Mach flow solver for direct numerical simulations (2024). https://arxiv.org/abs/2409.06404

Knaus, R., Pantano, C.: On the effect of heat release in turbulence spectra of non-premixed reacting shear layers. Journal of Fluid Mechanics **626** (2009) https://doi.org/10.1017/S0022112008005636

Lieuwen, T.C., Yang, V., Yetter, R.A.: Synthesis Gas Combustion: Fundamentals and Applications. CRC Press (2009). https://doi.org/10.1201/9781420085358

Lignell, D.O., Chen, J.H., Smith, P.J.: Three-dimensional direct numerical simulation of soot formation and transport in a temporally evolving nonpremixed ethylene jet flame. Combustion and Flame **155** (2008) https://doi.org/10.1016/j.combustflame.2008.05.020

Lindemann, F.A., Arrhenius, S., Langmuir, I., Dhar, N.R., Perrin, J., Lewis, W.C.M.: Discussion on the radiation theory of chemical action. Transactions of the Faraday Society **17** (1922) https://doi.org/10.1039/TF9221700598

Lysenko, D.A., Ertesvåg, I.S., Rian, K.E.: Numerical simulation of non-premixed turbulent combustion using the eddy dissipation concept and comparing with the steady laminar flamelet model. Flow, Turbulence and Combustion **93**(4), 577–605 (2014) https://doi.org/10.1007/s10494-014-9551-7

Mi, J., Nobes, D.S., Nathan, G.J.: Influence of jet exit conditions on the passive scalar field of an axisymmetric free jet. Journal of Fluid Mechanics **432**, 91–125 (2001) https://doi.org/10.1017/S0022112000003384

Minamoto, Y., Chen, J.H.: Dns of a turbulent lifted dme jet flame. Combustion and Flame **169** (2016) https://doi.org/10.1016/j.combustflame.2016.04.007

Moin, P., Mahesh, K.: Direct numerical simulation: A tool in turbulence research. Annual Review of Fluid Mechanics **30**, 539–578 (1998) https://doi.org/10.1146/annurev.fluid.30.1.539

Pantano, C.: Direct simulation of non-premixed flame extinction in a methane–air jet with reduced chemistry. Journal of Fluid Mechanics **514** (2004) https://doi.org/10.1017/S0022112004000266

Paykani, A., Chehrmonavari, H., Tsolakis, A., Alger, T., Northrop, W.F., Reitz, R.D.: Synthesis gas as a fuel for internal combustion engines in transportation. Progress in Energy and Combustion Science **90** (2022) https://doi.org/10.1016/j.pecs.2022.100995

Peters, N.: Turbulent Combustion. Cambridge Monographs on Mechanics. Cambridge University Press (2000). https://doi.org/10.1017/CBO9780511612701

Pitsch, H., Steiner, H.: Large-eddy simulation of a turbulent piloted methane/air diffusion flame sandia flame d. Physics of Fluids (2000) https://doi.org/10.1063/1.1288493

Poinsot, T., Veynante, D.: Theoretical and Numerical Combustion, 3rd edn. R. T. Edwards (2011)

Pope, S.B.: Turbulent Flows. Cambridge University Press (2000). https://doi.org/10.1017/CBO9780511840531

Salvadore, F., Bernardini, M., Botti, M.: Gpu accelerated flow solver for direct numerical simulation of turbulent flows. Journal of Computational Physics **235**, 129–142 (2013) https://doi.org/10.1016/j.jcp.2012.10.012

Scialabba, G., Davidovic, M., Attili, A., Pitsch, H.: Direct numerical simulation of soot break-through in turbulent non-premixed flames. Combustion and Flame **275** (2025) https://doi.org/10.1016/j.combustflame.2025.114093

Stewart, P.H., Larson, C.W., Golden, D.M.: Pressure and temperature dependence of reactions proceeding via a bound complex. 2. Application to $2CH_3 \rightarrow C_2H_5 + H$. Combustion and Flame **75** (1989) https://doi.org/10.1016/0010-2180(89)90084-9

Sung, C.-J., Law, C.K.: Fundamental combustion properties of H_2/CO mixtures: Ignition and flame propagation at elevated pressures. Combustion Science and Technology **180**(6), 1097–1116 (2008) https://doi.org/10.1080/00102200801963169

Thring, M.W., Newby, M.P.: Combustion length of enclosed turbulent jet flames. Symposium (International) on Combustion **4**(1), 789–796 (1953) https://doi.org/10.1016/S0082-0784(53)80103-7

Toro, E.: Riemann Solvers and Numerical Methods for Fluid Dynamics: A Practical

Introduction, (2009). https://doi.org/10.1007/b79761

Varga, T., Olm, C., Nagy, T., Zsély, I.G., Valkó, E., Pálvölgyi, R., Curran, H.J., Turányi, T.: Development of a joint hydrogen and syngas combustion mechanism based on an optimization approach. International Journal of Chemical Kinetics **48**(8), 407–422 (2016) https://doi.org/10.1002/kin.21006

White, F.M.: Fluid Mechanics, 7th edn. McGraw-Hill (2011)

Xu, G., Antonia, R.A.: Effect of different initial conditions on a turbulent round free jet. Experiments in Fluids **33**, 677–683 (2002) https://doi.org/10.1007/s00348-002-0523-7

Yaliwal, V.S., Banapurmath, N.R., Gireesh, N.M., Tewari, P.G.: Production and utilization of renewable and sustainable gaseous fuel for power generation applications: A review of literature. Renewable and Sustainable Energy Reviews **34** (2014) https://doi.org/10.1016/j.rser.2014.03.043

Yeung, P.K., Pope, S.B.: Lagrangian statistics from direct numerical simulations of isotropic turbulence. Journal of Fluid Mechanics **207** (1989) https://doi.org/10.1017/S0022112089002697

Supplementary Files

This is a list of supplementary files associated with this preprint. Click to download.

- Supplementarymaterial.zip